Hypersonic Point-to-Point Travel for the Common Man

Bislip, Carlos; Mooij, Erwin

Important note
To cite this publication, please use the final published version (if applicable).
Please check the document version above.

Hypersonic Point-to-Point Travel for the Common Man

Carlos Bislip and Erwin Mooij

1 Introduction

Hypersonic travel has historically been experienced exclusively by healthy and heavily trained individuals. The increased accelerations experienced are known to cause a variety of effects on human physiology, ranging from heavy breathing and discomfort to gravity-induced loss of consciousness (G-LOC). Furthermore, high speed travel has not been technologically feasible, nor economically viable for the population at large. However, advancements in both computational and rocket technology have shown glimpses of a broader cross section of the population being able to participate in what is known as *space tourism*. However, medical screenings and prior training, if not required, are strongly suggested.

The commercial aviation industry has advanced to the point where, for the most part, only individuals susceptible to lower ambient pressures are recommended to avoid travel. Though during a typical flight there are moments where the accelerations are larger than those experienced while at sea level and constant velocity, the portion of the population that cannot travel on an aircraft is effectively negligible. This mass availability is essential for cost reduction and economies of scale, both of which are key factors relevant to commercial airlines. Hence, even if hypersonic travel were technically feasible to the point that it became commonplace, it is reasonable to believe that without the inclusion of a significant portion of the population, any endeavour would most certainly remain economically out of reach for the common individual.

This chapter aims to delineate a framework in which the design space is explored with the goal of identifying a trajectory with hypersonic velocities, for a specified

C. Bislip · E. Mooij (✉)
Faculty of Aerospace Engineering, Delft University of Technology, Delft, The Netherlands
e-mail: e.mooij@tudelft.nl

route and vehicular configuration, where individuals could travel without health screenings and prior training. This effectively translates to a trajectory where the mechanical loads experienced by the passengers are analogous to those experienced while at sea level and constant velocity or a maximum total mechanical load of 1 g_0. However, due to the nature of the vehicle selected and the calculation of the g_0-loads, the 1 g_0 maximum is in effect an *increase* to values experienced while at sea level and constant velocity. To identify such a trajectory, a three degrees-of-freedom translational simulator is built in C++ with TU Delft Astrodynamics Toolbox (Tudat) and Parallel Global Multi-objective Optimiser (PaGMO) libraries. Tudat is an open-source C++ package that contains a set of publicly available libraries[1] of mathematical tools, environmental models, numerical integrators, and interpolators (linear and cube spline). PaGMO is '*an optimisation framework developed within the Advanced Concepts Team of the European Space Agency (ESA)*'.[2] It is an open-source software written in C++ that enables automatic parallelisation of its optimisers and includes evolutionary algorithms that can be used with multiple objectives, such as NSGA-II and MOEA/D (DE) [1–3].

The simulator, presented in Sect. 2, employed an open-loop guidance system with idealised navigation and control systems, where node control is the control method [4, 5]. For use with the evolutionary algorithms, the decision vector parameters are presented in Sect. 3, while the fitness vector components are discussed in Sect. 4. As the design space is not well understood, it is unknown how effective these available evolutionary algorithms would be. Hence, the extensive design space exploration discussed in Sect. 5 is performed to inform the selection of a genetic algorithm, an objective function case, and a given number of independent variables.

Finally, in Sect. 6, the trajectory optimisation will be performed via two approaches. One approach performs separate optimisations for each phase, denoted throughout as *decoupled*. Within the decoupled approach, the descent phase is performed for a variety of starting points. The ascent phase optimisation is then linked to its corresponding decoupled descent phase, with the goal of producing a linkable trajectory. The alternate approach combines the ascent and descent phases into one large problem, denoted throughout as *coupled*. A sub-optimal trajectory is found and used as a reference for localised optimisation, followed by a detailed analysis. Concluding remarks and suggestions for further study are given in Sect. 7.

2 Simulation Model

The most relevant components of the simulation model are sequentially discussed. These include the reference vehicle and mission in Sects. 2.1 and 2.2. This is followed by a summary of the simulated flight dynamics and aerodynamic heating in

---

Sects. 2.3 and 2.4. Finally, a key discussion about the vehicle's guidance is presented in Sect. 2.5. It is important to note that though not presented nor discussed, the simulation model has been successfully validated against known reference missions.

2.1 Reference Vehicle

The reference vehicle is the second stage of the Sänger II system [7]. Though the first stage was not intended for passenger transport, it did consider an optional second stage for this express purpose. Known as the Hypersonic ORbital Upper Stage (HORUS), the second stage would be air launched with the goal of reaching orbit. The HORUS stage design experienced a series of versions. Of these, the most relevant are the HORUS-2B and HORUS-3B.

The HORUS-2B, which provides the overall geometric features shown in Fig. 1a, was a manned winged reusable vehicle with a crew of 2–4 and a small cargo payload. In this configuration, the vehicle would provide Space Station support, which was at the time estimated to be at an orbit with an altitude of 450 km at an
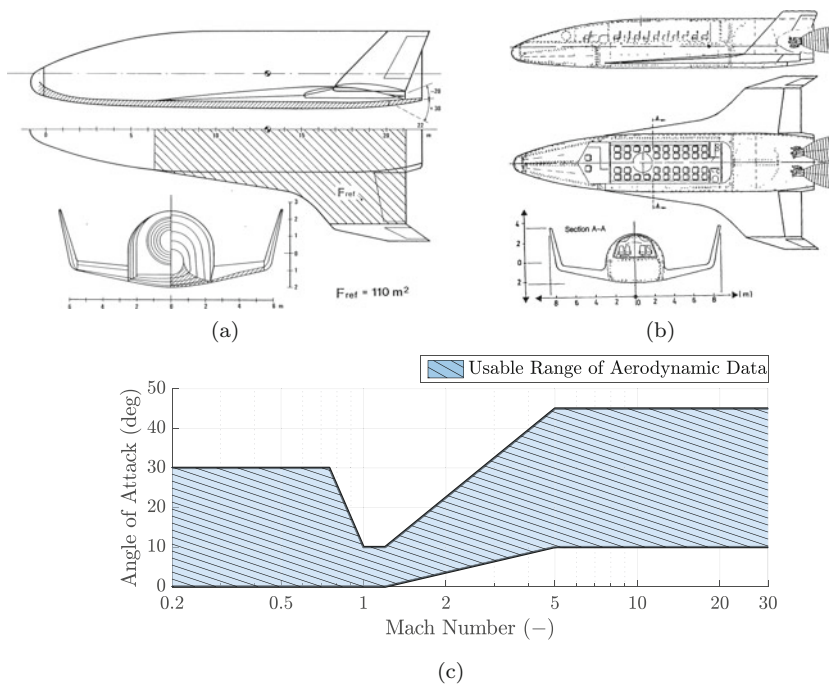

Fig. 1 DLR's HORUS cross section, passenger concept, and trimmable envelope [7, 8, 10]. (**a**) HORUS-2B cross section. (**b**) Passenger HORUS-3B conceptual design. (**c**) Trimmable aerodynamic envelope

Table 1 HORUS
characteristics [7, 8]

Description	Units	Value
MBB ATC-700 Engine	–	2
Max engine thrust (T_{max})	kN	700
Specific impulse	s	472
Propellant mass	kg	65,000
Max payload mass	kg	7000
Re-entry mass	kg	26,029
I_{xx}	kg·m^2	119,000
I_{yy}	kg·m^2	769,000
I_{zz}	kg·m^2	806,000

inclination of 28.5°. As the HORUS-3B, shown in Fig. 1b, the vehicle would be capable of cabin modifications that would facilitate accommodating 36 passengers for the explicit purpose of space tourism. This version had a complete propulsion system with 65 Mg of propellant and 2 rocket engines. Each engine had a thrust of 700 kN and a specific impulse I_{sp} of 472 s [7].

The HORUS-3B engine characteristics will be used with the HORUS-2B aerodynamic database provided by MBB [8] and discretised by Mooij [9]. The vehicle's trimmable envelope is illustrated in Fig. 1c, whereas Table 1 presents a summary of the vehicle's characteristics.

2.2   Reference Mission

The reference mission to simulate will begin post-separation of the second stage at an altitude h_0 of 35 km and a velocity of Mach 6.6 with an initial heading χ_0 to the destination. The reference origin is the Koninklijke Luchthaven Schiphol (Amsterdam Airport Schiphol), and the reference destination is Washington Dulles International Airport. The simulation is terminated upon reaching the terminal area defined by a distance of 0.75° from the reference destination coordinates. At this distance, the Terminal Area Energy Management (TAEM) system would guide the system in the final phases of its flight, analogous to the Space Shuttle's Orbiter [15]. This is beyond the scope of the present work. A great circle is created by the reference origin and destination to define the trajectory's initial angular distance-to-go $\theta_{ToGo,0}$, equal to about 55.82°.

2.3   Flight Dynamics

The translational equations of motion of the system are defined by the gravitational force, the aerodynamic forces, and the resultant of all thrust forces. These forces are all defined in their own reference frames, which requires them to be transformed

to the inertial frame, $\mathcal{F}_I$, through a corresponding rotation matrix $\boldsymbol{C}$. The rotation matrix convention is such that the left arrow symbol $\leftarrow$ indicates the direction of rotation. For example, $\boldsymbol{C}_{I \leftarrow A}$ would rotate a vector from the aerodynamic frame $\mathcal{F}_A$ to the inertial frame $\mathcal{F}_I$.

$$\frac{d\boldsymbol{V}_I}{dt} = [\ddot{x}_I, \ddot{y}_I, \ddot{z}_I]^T = \frac{1}{m} \left(\boldsymbol{F}_{g,I} + \boldsymbol{F}_{A,I} + \boldsymbol{F}_{T,I} \right) \tag{1a}$$

$$= \frac{1}{m} \left(\boldsymbol{C}_{I \leftarrow V} \boldsymbol{F}_{g,V} + \boldsymbol{C}_{I \leftarrow A} \boldsymbol{F}_{A,A} + \boldsymbol{C}_{I \leftarrow B} \boldsymbol{F}_{T,B} \right) \tag{1b}$$

$$\frac{d\boldsymbol{r}_{cm,I}}{dt} = [\dot{x}_I, \dot{y}_I, \dot{z}_I]^T = \boldsymbol{V}_I \tag{2}$$

Though the force terms are each subsequently discussed in more detail, the final set of equations can then be put together as shown in Eqs. (1a) and (2). Equation (1a) expresses the time rate of change of the vehicle's inertial frame velocity $\boldsymbol{V}_I$ in Cartesian coordinates yielding the vehicle's inertial frame acceleration, also in Cartesian coordinates. This acceleration, expressed as the second time derivative of position (i.e. $\ddot{x}_I$, $\ddot{y}_I$, and $\ddot{z}_I$), is in turn equal to the sum of inertial frame forces divided by the mass m. Similarly, Eq. (2) expresses the time derivative of the position of the vehicle's inertial frame centre of mass $\boldsymbol{r}_{cm,I}$ in Cartesian coordinates yielding the vehicle's inertial frame velocity $\boldsymbol{V}_I$, also in Cartesian coordinates and as the first time derivative of position (i.e. $\dot{x}_I$, $\dot{y}_I$, and $\dot{z}_I$).

The gravitational acceleration can be defined with first-order approximations, such as the Earth's flattening. The Earth's flattening can be mostly accounted for with the J_2 zonal harmonic and equivalent to $1.082626523 \times 10^{-3}$ [11]. To include these effects, the gravitational acceleration is defined with spherical coordinates in the vertical frame, $\mathcal{F}_V$.

$$\boldsymbol{F}_{g,V} = m\boldsymbol{g}_V = m \left[g_n, 0, g_d \right]^T \tag{3}$$

$$g_n = -3J_2 \frac{\mu}{r^2} \left(\frac{R_E}{r} \right)^2 \sin\delta \cos\delta \tag{4}$$

$$g_d = \frac{\mu}{r^2} \left[1 - \frac{3}{2} J_2 \left(\frac{R_E}{r} \right)^2 \left(3\sin^2\delta - 1 \right) \right] \tag{5}$$

The gravitational force the Earth imposes on an object is shown in Eq. (3). In Eqs. (4) and (5), μ is the Earth's gravitational parameter equal to 398600.440 km^3/s^2, g_n is the gravitational acceleration in the north direction, and g_d is downwards along the radial direction. Furthermore, r is the radial distance of the reference vehicle to the centre of the Earth and δ is the geocentric latitude. The dependency on longitude is not present due to an assumed rotational symmetry of the central mass M of the Earth [11, 12].

The aerodynamic drag, D, side force, S, and lift, L, are a function of velocity V, angle of attack α, and sideslip angle β. These terms are defined in the aerodynamic frame based on airspeed. Though defined in the airspeed frame $\mathcal{F}_{A,A}$, they must be used in the groundspeed frame $\mathcal{F}_{A,G}$. However, since wind effects are not considered, they may be used as is to calculate the vehicle's dynamic pressure $\bar{q} = \frac{1}{2}\rho V^2$ (where ρ is the local density) and the aerodynamic coefficients for drag C_D, side force C_S, and lift C_L.

$$\boldsymbol{F}_{A,A} = -[D, S, L]^{\mathrm{T}} = -\bar{q}S_{ref}[C_D, C_S, C_L]^{\mathrm{T}} \tag{6}$$

Equation (6) presents the relevant expression for the aerodynamic forces. As side forces are not considered, through the assumption of $\beta = 0$, only the drag and lift coefficients C_D and C_L are determined from the aerodynamic database. They are, however, a function of the vehicle's Mach number M, angle of attack, body flap deflection angle δ_b, and elevon deflection angle δ_{el}. The deflection angles are determined to maintain a trimmed flight.

Regarding the thrust force term, the vehicle is modelled to have a single commanded thrust force $T_c = \xi T_{\max}$ that is applied through the $\hat{x}$-axis of the body frame, $\mathcal{F}_B$. The commanded thrust force is the combined value of the maximum available thrust from the rocket engines and a throttle setting ξ, which will be explained further in Sect. 2.5.

$$\boldsymbol{F}_{T,B} = [T_c, 0, 0]^{\mathrm{T}} \tag{7}$$

2.4 Aerodynamic Heating

The heat input will be evaluated with a simplified expression known as the *Chapman Equation* [13]. The expression evaluates the convective heat flux per unit area at the stagnation point of the vehicle's nose, which has a known radius R_N.

$$q_c = C\rho^n V^m \left(1 - \frac{T_w}{T_{w_{ad}}}\right) \tag{8}$$

$$q_{rad} = \varepsilon\sigma T_w^4 = q_c \tag{9}$$

$$T_w = \sqrt[4]{\frac{q_c}{\varepsilon\sigma}} \tag{10}$$

Equation (8) is the hot-wall generalised form of Chapman's Equation, where $n = 0.5$, $m = 3.15$, and $C = 1.83 \times 10^{-8}R_N^{-0.5}$. The ratio of wall temperatures (T_w and $T_{w_{ad}}$) is determined by assuming thermal equilibrium and equating Eq. (8) with the radiative heat flux, as shown in Eq. (9). This requires an iterative process with an initial assumed value of either q_c or T_w and sequentially updating each other

until convergence [14]. In Eq. (10), ε is the surface emissivity and σ is the *Stefan-Boltzmann constant*. Following simplified and effective methods, the integrated heat load will be determined as the numerical integral of the heat flux q_c.

2.5 Guidance

Typical control methods used in aerospace applications use some form of feedback to apply control corrections about a known reference value (see Fig. 2). However, the current problem does not have known reference values for any control parameter. Additionally, the ideal controller is to have an instantaneous effect on command settings and aerodynamic trim. These considerations give reason to the use of node control, which utilises a set of control nodes to relate control parameters to an arbitrary independent variable. The control parameters are defined at each control node and interpolated at all other points. This brings forth the issues of identifying the number of control nodes, their relative locations, the independent variable, and the interpolation method.

The number of control nodes and their relative locations have a direct and significant effect on the design space and the resulting trajectory. Regarding the design space, a control node requires the definition of each applicable control parameter. A maximum of three control parameters are to be on either ascent or descent: angle of attack α, bank angle σ, and throttle setting ξ. These parameters, being defined at each control node, then require an associated value in the independent variable space.

Figure 3 illustrates the time histories of a series of variables for a typical coupled trajectory that could be considered as candidates for the independent variable. The general expectation of the independent variable is to be well behaved and monotonically increasing/decreasing. The overall purpose of this desired behaviour is to minimise oscillations (well behaved) and avoid ambiguities (monotonic) in the evaluation of the control parameters. In relation to the application in the problem, it is also known that a significant amount of energy must be steadily dissipated to
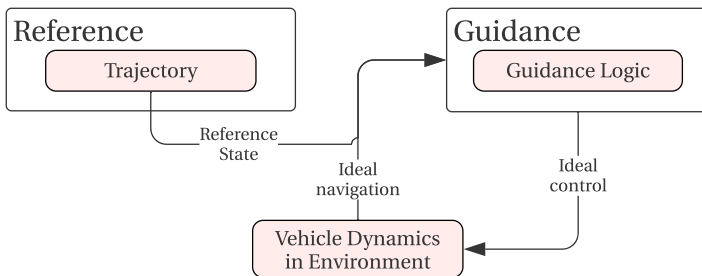

Fig. 2 Pseudo open-loop GNC system with ideal navigation module and ideal control module
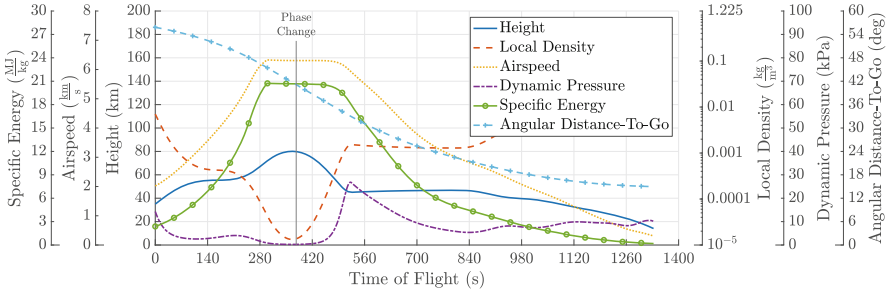
Fig. 3 Typical coupled trajectory time histories of candidate control node independent variables

maintain a reduced increase in g_0-loads. This requires the independent variable to be dynamic enough to change the control parameters as needed yet sufficiently stable as to not generate sudden changes nor oscillations.

The Space Shuttle's Orbiter landing guidance system, also known as the TAEM system, used the concept of *energy height* [15]. The successful Orbiter landings indicate that this concept indeed satisfies the requirements, particularly due to the combination of the vehicle's height and velocity into a single value. Furthermore, the expression may also be known as specific energy, effectively removing any mass term from the relation. The formulation, based on a flat Earth, has clear differences from the expression that corresponds to a spherical Earth. However, the normalised distributions of the separate formulations, as implemented within any particular trajectory, will be equivalent. The variable's utility with node control, as applied to re-entry vehicles, has been previously demonstrated by Mooij and Hänninen [4], Dijkstra et al. [5], and Hess and Mooij [6].

$$\hat{E} = \frac{E}{E_{\max}} = \frac{1}{E_{\max}} \left(g_0 h + \frac{1}{2} V^2 \right) \tag{11}$$

The maximum specific energy, $E_{\max}$ in Eq. (11), is determined with the maximum height $h_{\max}$ and maximum airspeed $V_{\max}$ parameters defined in Sect. 3. Though these could be coupled into a single optimisation parameter encompassing the entire range generated by the separate parameters, it was chosen to not do so to allow an additional degree of freedom. Naturally, since $E_{\max}$ is effectively an optimisation parameter that is defined prior to the evaluation of the trajectory and is also taken as the reference value, the useful range of values will also be affected. If at any point a trajectory's scaled specific energy goes beyond 1, all evaluated control parameters would remain at their corresponding value of a scaled specific energy value of 1.

Figure 4 illustrates the scaling transformation on the specific energy time history of a typical trajectory, where the maximum scaled specific energy $\hat{E}_{\max,\text{actual}}$ evaluates to a value of 0.93. It is important to note that $E_{\max}$ is set with initialised values and is not influenced from the trajectory's values. Initial and final specific
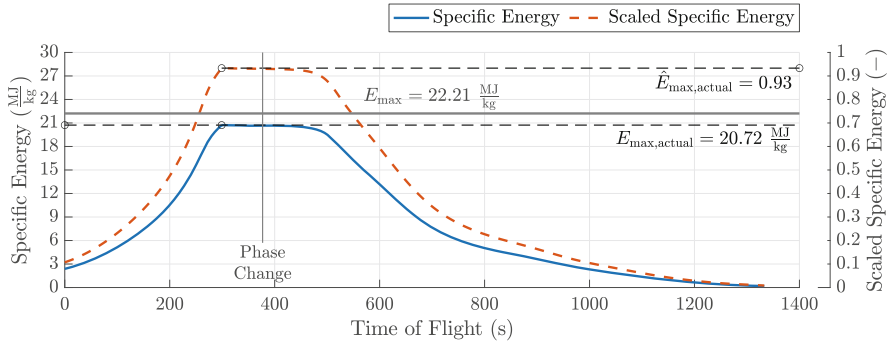
Fig. 4 Illustration of scaling $E \rightarrow \hat{E}$ [$h_{\max} \approx 119$ km, $V_{\max} \approx 6.5 \frac{\text{km}}{\text{s}}$]

Table 2 Nominal initial and final specific energy state source parameters

Description	Units	Initial	Final
Mach	–	6.6	2.5
Height	km	35.0	25.0
Specific energy	MJ/kg	2.38	0.518
Scaled specific energy[a]	–	0.107	0.023

[a] Based on sample data from Fig. 4

energy states need not be fixed either; if fixed, four parameters are removed from the design space. The relevant values are presented in Table 2, where Mach numbers are converted to velocity with the NRLMSISE-00 atmospheric model. The sample scaled specific energy values used a scaling factor of $E_{\max} = 22.21 \frac{\text{MJ}}{\text{kg}}$, as shown in Fig. 4.

The previous work by Dijkstra et al. [5] concluded the Non-Uniform Independent Node (NUIN) method to be applicable for trajectory optimisation. Its implementation requires $n - 1$ initial values in the range of [0, 1] for n nodes. These values are then cumulatively summed per each control node i in a node location vector, which is then scaled by the maximum value (the total sum). This procedure implicitly generates the control node intervals and ensures all node locations are within [0, 1]

$$\boldsymbol{x} = [x_1, x_2, \ldots, x_{n-1}] \in [\, 0, 1 \,] \tag{12}$$

$$x_{\text{node},i} = \begin{cases} 0 & \text{if } i = 1 \\ \displaystyle\sum_{j=2}^{i} x_{j-1} & \text{if } i > 1 \end{cases} \tag{13}$$

$$\hat{x}_{\text{node},i} = \frac{x_{\text{node},i}}{x_{\text{node},n}} \tag{14}$$

$$\hat{E}_{\text{node,mapped},i} = \left(\hat{E}_{\max} - \hat{E}_{\min} \right) \hat{x}_{\text{node},i} + \hat{E}_{\min} \tag{15}$$
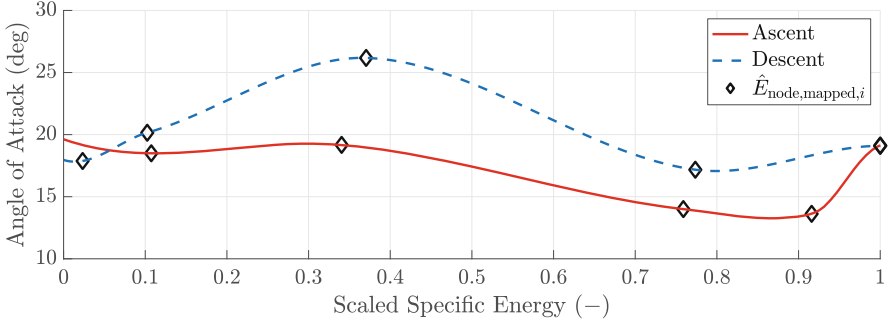
Fig. 5 Node mapping to the energy domain is followed by the application of guidance matrix values and the implementation of Hermite interpolation

$$\hat{E}_{\min} = \begin{cases} \hat{E}_{\text{initial}} & \text{if ascent} \\ \\ \hat{E}_{\text{final}} & \text{if descent} \end{cases} \tag{16}$$

$$\boldsymbol{\Gamma} = \begin{bmatrix} \hat{E}_{\min} & \alpha_1 & \sigma_1 & \xi_1 \\ \hat{E}_2 & \alpha_2 & \sigma_2 & \xi_2 \\ \vdots & \vdots & \vdots & \vdots \\ \hat{E}_{n-1} & \alpha_{n-1} & \sigma_{n-1} & \xi_{n-1} \\ \hat{E}_{\max} & \alpha_n & \sigma_n & \xi_n \end{bmatrix} \tag{17}$$

The process is illustrated by evaluating Eqs. (12) through (14), followed by mapping the node locations to the energy domain through Eq. (15). The resulting guidance matrix $\boldsymbol{\Gamma}$ for each phase will then contain the nodal scaled specific energy as it is related to each control parameter initialisation. Equation (17) shows the structure of the guidance matrix created for each trajectory phase, where $\hat{E}_{\max}$ is defined by Eq. (16).

As a piecewise polynomial, high degree polynomials could induce large oscillations (commonly referred to as *Runge's Phenomenon*). Figure 5 illustrates that this issue will be addressed by implementing cubic Hermite interpolators with smooth and continuous first derivatives at the endpoints, as developed by Han and Guo [16].

2.5.1 Skip Suppression

During descent, the flight-path angle will be controlled to ensure that the vehicle does not bounce back out of the atmosphere or experience excessive skipping. This is achieved by elaborating further on the derivation presented by Vinh et al. [17], followed by setting flight-path angle rate $\dot{\gamma} = 0$ if the flight-path angle $\gamma \geq 0$ and identifying the corresponding values of the remaining parameters. Neither thrust

vector control (TVC), such as gimballing, nor side forces are included. These considerations allow for the derivation of an expression from which the bank angle can be determined. However, this bank angle may be different from the operational parameter that would be determined via node control.

$$\cos \sigma_{ss} = \frac{m}{L + T_c \sin \alpha} \left(g_d \cos \gamma - g_n \sin \gamma \cos \chi \cdots \right.$$

$$\cdots - \omega_E^2 r \cos \delta \left(\cos \delta \cos \gamma + \sin \gamma \sin \delta \cos \chi \right) \cdots$$

$$\left. \cdots - \frac{V^2}{r} \cos \gamma - 2\omega_E V \cos \delta \sin \chi \right) \tag{18}$$

$$\sigma_c = \begin{cases} \text{if descent \& } \rho > \rho_{\min} & \begin{cases} \sigma & \text{if } \gamma < 0.0 \\ \sigma_{ss} & \text{if } \gamma \geq 0.0 \end{cases} \\ \text{otherwise} & 0.0 \end{cases} \tag{19}$$

The resulting expression based on the Vinh et al. [17] derivation is shown in Eq. (18). The skip suppression bank angle σ_{ss} is shown to be a function of previously discussed forces, such as lift L, thrust T_c, and gravity in its components g_n and g_d. Additional required parameters are the vehicle's mass m, airspeed V, angle of attack α, flight-path angle γ, heading angle χ, geocentric latitude δ, and radial distance r from the Earth's centre. Finally, though potentially having negligible effects, the Earth's angular speed ω_E of $7.2921150 \times 10^{-5} \frac{\text{rad}}{\text{s}}$ is largely included for completion.

Equation (19), on the other hand, introduces the commanded bank angle logic. The expression shows that the bank angle will be fixed to zero during the ascent phase. During the decent phase, banking of any kind will be commanded if a minimum local density is being met. The said banking will be determined by node control if the flight-path angle γ is lower than zero or by skip suppression with Eq. (18) if the flight-path angle γ is non-negative.

2.5.2   Lateral Guidance

During descent, the vehicle will use the angle of attack to dissipate excess energy and the bank angle to ensure that a path that continuously decreases in altitude. Though a mild slip is not expected to be problematic, the oscillatory behaviour could also bring about undesired oscillatory evaluations of the guidance variables. Regardless, these considerations would not guide the vehicle towards its intended destination.

The vehicle's lateral guidance is implemented by restricting the heading error χ_e with a so-called heading error dead-band $\chi_{e,db}$ and a *bank reversal*. The heading error dead-band $\chi_{e,db}$ is taken to be a function of angular distance-to-go θ_{ToGo} from the intended target. The bank reversal is a sign change of the bank angle that occurs

if the magnitude of the heading error continues to increase beyond its corresponding dead-band. However, the goal is to reach the TAEM, which would allow the lateral guidance to aim at any point on the boundary of the TAEM. This creates a moving target that is bound by tangential great circles generated from the vehicle's location.

Figure 6 illustrates the arbitrary location of the vehicle at point A and the central target at point B. The circle around B represents the TAEM region, which is tangent to the great circles that originate from A at T_1 and T_2. The heading angles required to follow the great circles would define χ_{T_1} and χ_{T_2}, and any heading angle within these bounds would indicate that the vehicle is aiming towards the TAEM region.

$$\chi_e = \begin{cases} 0 & \text{if } \chi_{T_1} \leq \chi \leq \chi_{T_2} \\ \chi - \chi_{T_1} & \text{if } |\chi - \chi_{T_1}| < |\chi - \chi_{T_2}| \\ \chi - \chi_{T_2} & \text{if } |\chi - \chi_{T_2}| < |\chi - \chi_{T_1}| \end{cases} \qquad (20)$$
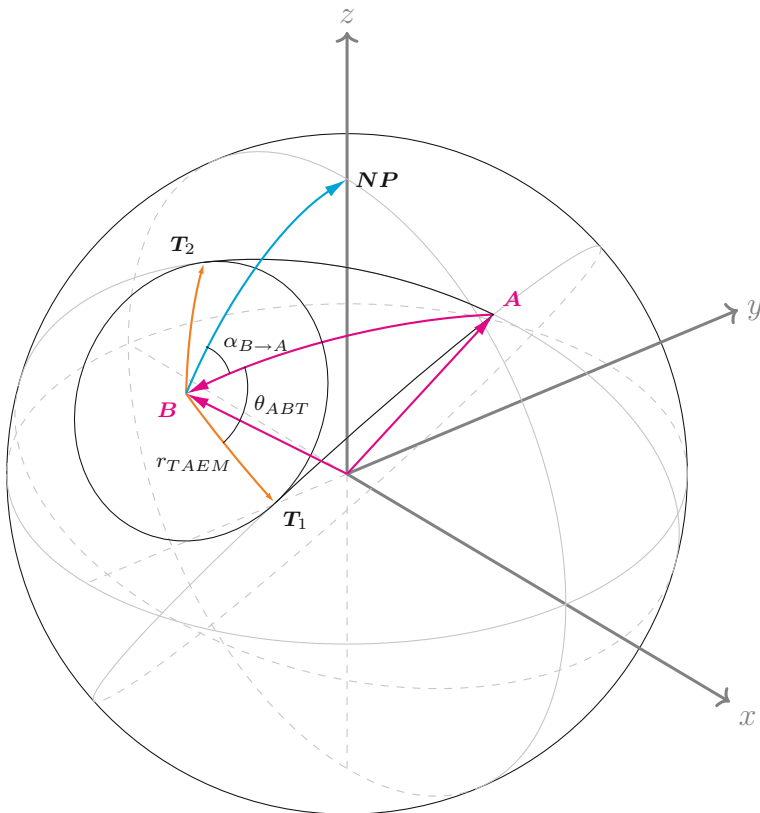

Fig. 6 Geometry for deriving the heading to tangent points on an arbitrary circle on the surface of a sphere

Equation (20) shows that a heading error only occurs when the vehicle is not aiming towards the TAEM region. To identify these bounds, the internal angles θ_{ABT_1} and θ_{ABT_2} are identified by using the modified Gram–Schmidt procedure. Vector algebra and Cartesian coordinates are used through the implementation of the procedure outlined below.

$$U_1 = A - \left(\frac{A \cdot \hat{B}}{\hat{B} \cdot \hat{B}} \right) \cdot \hat{B} \tag{21}$$

$$\hat{U}_1 = \frac{U_1}{\|U_1\|} \tag{22}$$

$$\hat{B} = \frac{B}{\|B\|} \tag{23}$$

$$\theta_{ABT_1} = \theta_{ABT_2} = \theta_{ABT} = \arccos \left[\frac{(A \cdot B) \tan r_{\text{TAEM}}}{A \cdot \hat{U}_1} \right] \tag{24}$$

$$\alpha_{B \rightarrow T_{1,2}} = \alpha_{B \rightarrow A} \pm \theta_{ABT} \tag{25}$$

Equations (21) through (23) facilitate the calculation of the internal angle θ_{ABT} with Eq. (24). In this equation, r_{TAEM} is the radius of the TAEM region and effectively the distance from point B at which the tangent points are located. To then identify the coordinates of the tangent points, the azimuth $\alpha_{B \rightarrow A}$ from the central target (point B) to the vehicle (point A) is first determined. Equation (25) is then used to calculate the heading $\alpha_{B \rightarrow T_{1,2}}$ to tangent points T_1 and T_2. Once the coordinates of T_1 and T_2 are known, the bounding heading angles of the vehicle (χ_{T_1} and χ_{T_2}) and the corresponding dynamic target angular distance-to-go $\theta_{ToGo,dyn}$ are calculated. In the event that $\chi_e = 0$, as determined with Eq. (20), the vehicle would have a heading angle that aims towards the TAEM region. In this case, a similar approach is used to determine the coordinates of the TAEM boundary intersection point, which then allows for the calculation of the angular distance $\theta_{ToGo,dyn}$.

3 The Decision Vector

The approach to the current problem will be to structure the decision vector into two sets of optimisation parameters: *non-nodal* and *nodal* parameters. Both sets are a function of the trajectory phase to be evaluated, especially when comparing coupled and decoupled decision vectors.

All parameters not associated with node control are shown in Table 3. Their associated exploration bounds are provided for each trajectory type. From these non-nodal parameters, the additional mass $m_{\text{additional}}$, the phase termination distance ratio ζ, and the decoupled descent distance-to-go ratio $\hat{\theta}_{ToGo,i}$ warrant additional context.

Table 3 Non-nodal parameters and exploration bounds

Description	Parameter	Units	Exploration bounds Ascent Lower	Ascent Upper	Descent Lower	Descent Upper	Coupled Lower	Coupled Upper
Initial flight-path angle	γ_0	deg	1.5	8.0	−89.9	0.0	1.5	8.0
Maximum airspeed	V_{max}	km/s	a		3.0	7.0	3.0	7.0
Maximum height	h_{max}	km	a		70.0	200.0	70.0	200.0
Additional mass	$m_{additional}$	Mg	a		0.0	30.0	0.0	30.0
Phase termination distance ratio	ζ	–	a		–		0.1	0.7
Ascent optimisation airspeed	$V_{f,ascent}$	km/s	a		–		–	
Ascent optimisation height	$h_{f,ascent}$	km	a		–		–	
Final ascent flight-path angle	γ_f	deg	a		–		–	
Initial distance-to-go ratio[b]	$\hat{\theta}_{ToGo,i}$	–	–	–	0.3	0.9	–	
Descent optimisation airspeed	$V_{0,descent}$	km/s	–		0.75	7.0	–	
Descent Optimisation Height	$h_{0,descent}$	km	–		35.0	200.0	–	

[a] Fixed to corresponding linking value determined by decoupled descent optimisation
[b] Will be evaluated at fixed intervals of 0.15

Though nominal operations of the reference vehicle would have taken it to orbit, the current implementation not only limits the total mechanical loads but might also require longer operations within a thicker atmosphere. The possibility of increased propellant mass is then considered by also increasing the vehicle's dry mass as a function of the additional mass parameter.

$$m_{dry_{actual}} = m_{dry}\left[1 + 0.3\left(\frac{m_{additional}}{m_0}\right)\right] \tag{26}$$

The phase termination distance ratio ζ is used during the ascent phase as a necessary condition before terminating. It means that a portion of the initial central target angular distance-to-go $\theta_{ToGo,0}$ must be travelled before the next phase can commence. This translates to the minimum angular distance required $\theta_{required}$, which is the minimum angular distance to travel from the destination coordinates.

$$\zeta = \left(\frac{\theta_{required}}{\theta_{ToGo,0}}\right) \tag{27}$$

The initial decoupled descent distance-to-go ratio $\hat{\theta}_{ToGo,i}$ parameter is only used for a decoupled descent phase to fix the initial location of the vehicle with respect to the central target. The initial angular distance-to-go $\theta_{ToGo,i}$ is then the angular distance from the central target at which the simulation begins.

$$\hat{\theta}_{ToGo,i} = \left(\frac{\theta_{ToGo,i}}{\theta_{ToGo,0}}\right) \tag{28}$$

Table 4 Nodal parameters and exploration bounds

			Decoupled				Coupled			
			Ascent		Descent		Ascent		Descent	
Description	Parameter	Units	Lower	Upper	Lower	Upper	Lower	Upper	Lower	Upper
Angle of attack	θ	deg	10.0	20.0	0.2	50	10.0	20.0	0.0	50
Bank angle	σ	deg	–		0.0	89.0	–		0.0	89.0
Throttle setting	ξ	–	0.2	1.0	–		0.2	1.0	0.2	1.0

Table 5 Phase termination conditions

			Condition	
Description	Parameter	Units	Ascent	Descent
Ascent phase termination[a]	Eq. (29)	–	TRUE	–
Minimum allowable mach number	M_{min}	–	–	1.05
Minimum allowable height	h_{min}	km	$\frac{9}{10} h_0$	10.0
Minimum angular distance from central target	$\theta_{ToGo,min}$	deg	0.75	
Change in Angular distance from central target[b]	$\Delta\theta_{ToGo}$	deg	>0	

[a] Not applicable to decoupled ascent trajectories
[b] Used to indicate that the vehicle is travelling away from the central target

Table 4 presents the nodal parameters along with their general bounds as they are used in both decoupled and coupled evaluations. Though they are similar, the distinction lies in the idea that in a decoupled descent phase it is assumed that there is no more propellant mass available, whereas a coupled descent phase may still have leftover propellant from its coupled ascent phase.

Table 5 presents the phase termination conditions required throughout the evaluation of any decision vector. The table first references the necessary condition for a phase change in either a coupled trajectory or the ascent phase of a decoupled trajectory type.

$$\left(\hat{\theta}_{ToGo} \geq \zeta\right) \wedge (\gamma \leq 0) \wedge (\dot{\gamma} \leq 0) \rightarrow \text{Terminate ascent phase} \tag{29}$$

Equation (29) shows that a combination of three conditionals must be simultaneously met. The first condition being that $\hat{\theta}_{ToGo}$ must be equal or greater than ζ, which is the phase termination distance ratio defined in Eq. (27). This means that the vehicle must have first travelled a minimum distance before allowing a phase change. The second and third conditionals indicate that the vehicle's flight-path angle, γ, and corresponding rate, $\dot{\gamma}$, must both be equal to or lesser than zero. These mean that the vehicle must aim towards the Earth's surface without levelling back to a horizontal flight.

The lowest Mach number the descent phase will evaluate, M_{min}, is due to the reference vehicle's aerodynamic database not being defined for subsonic velocities. The lowest possible heights are included to terminate ascent phases that neither maintain nor increase the vehicle's height and to terminate descent phases that have

descended far beyond the height required for nominal TAEM interface conditions (see Table 2 for more details).

4 The Fitness Vector

The evolutionary algorithms available within PaGMO use a combination of objective functions, equality constraints, and inequality constraints to define an individual's fitness. For simplicity, the current implementation will focus on the objective functions determined by calculating a series of cost functions, constraint violations, and penalties that must be minimised. The corresponding expressions are computed according to the nature of the variables in question. Each value is scaled by a relevant limiting value, yielding a series of non-dimensional values, which can then be summed in different combinations for the fitness vector.

The costs have been defined to minimise the total angular distance-to-go, the total propellant mass, and the integrated heat load.

$$C_{\theta_{ToGo}} = 100\hat{\theta}_{ToGo,f} = 100\left(\frac{\theta_{ToGo,f}}{\theta_{ToGo,0}}\right) \tag{30}$$

$$C_{mass} = 100\left(\frac{m_{dry_{actual}} - m_{dry}}{m_{dry}}\right) + \frac{|V_0 - V_{max_{actual},a}|}{I_{sp}g_0 \ln\left(m_{0_{actual}}/m_{f,a}\right)} \tag{31}$$

$$C_Q = \frac{1}{t_{tof}q_{c,a}} \sum^{N} q_c\left(t\right) \Delta t \tag{32}$$

Constraint violations are used for all constrained variables, such as the g-load, dynamic pressure, bending moment, and nose-cone stagnation heat flux. These constraints, summarised in Table 6, would produce a violation only if the variable in question goes beyond the imposed constraint. The generic form is given by

Table 6 Summary of operational constraints

Description	Symbol	Units	Value	Source
Total g_0-Load	n_a	g_0	1.0	Current study
Dynamic pressure	$\bar{q}_a$	kPa	25.0	a
Bending moment	$(\bar{q}\alpha)_a$	kPa·deg	250.0	a
Stagnation heat flux	$q_{c,a}$	kW/m^2	700.0	a
Directional jerk[b]	j_a	m/s^3	2.0[b]	c

[a] See Dirkx and Mooij [18]
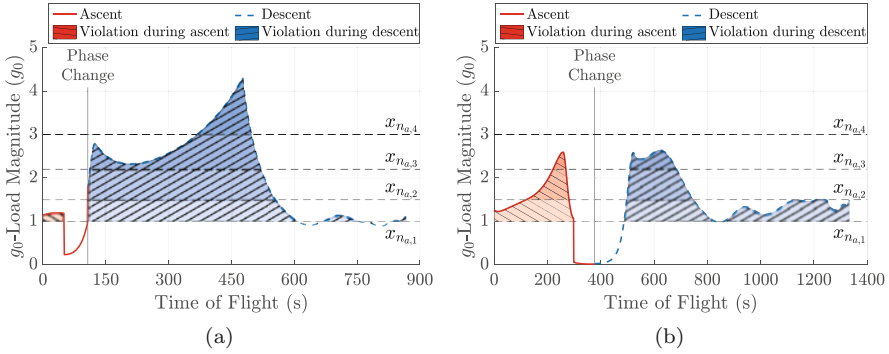[b] Secondary constraint, not enforced
[c] See ISO [19]

Fig. 7 Sample data for computation of constraint violations. (**a**) High peak low duration violation. (**b**) Low peak long duration violation

$$V_{\mathrm{c}} = \frac{x_{\max} - x_{\mathrm{c}}}{x_{\mathrm{c}}} + \frac{\sum_{i=1}^{n} (x_i - x_{\mathrm{c}}) \, \Delta t}{t_{tof} \cdot x_{\mathrm{c}}} \tag{33}$$

where the first term in Eq. (33) corresponds to the effect of the maximum constraint violation. The second term corresponds to the effect of the magnitude of each individual violation along with its duration throughout the trajectory, i.e., the area bounded by the portions of the curve that are beyond the constraint and the constraint line. Furthermore, Eq. (33) will be applied separately to each trajectory phase due to the difference in expected dynamics and operating parameters.

Figure 7 illustrates the combined effects of the duration of a phase, the overall trends, and the constraints being imposed, as expected from Eq. (33). Figure 7a shows how increased values can have a persistent effect that may be reduced by a low duration, whereas Fig. 7b shows how lower values can have a more significant resulting effect if prolonged throughout the trajectory. It is also possible to see the difference in relative calculation throughout each trajectory phase, accentuating the importance of calculating separate values for each phase.

Additional penalties are incurred for undesired trajectory characteristics. These include flight-path angles that have the 'wrong sign' during each phase and non-monotonic scaled specific energy profiles. The rationale for the flight-path angles is to avoid opposing changes in elevation during each trajectory phase, while the monotonically increasing/decreasing profiles would ensure unique evaluations of the guidance variables determined through node control.

$$P_{\gamma} = \frac{1}{360} \left| \left(x_{\max} + \frac{\sum_{i=1}^{n} x_i \Delta t}{t_{tof}} \right) \right| \quad \begin{cases} \text{if ascent,} & \forall x < 0 \\ \text{if descent,} & \forall x > 0 \end{cases} \tag{34}$$

$$P_{\hat{E}} = \sum_{i=2}^{n} |x_i - x_{i-1}| \quad \begin{cases} \text{if ascent,} & x_i < x_{i-1} \\ \text{if descent,} & x_i > x_{i-1} \end{cases} \tag{35}$$

Simply put, during ascent, it is desired to have non-negative flight-path angles and a monotonically increasing scaled specific energy profile, while during descent it is desired to have non-positive flight-path angles and a monotonically decreasing scaled specific energy profile. These characteristics can be determined from the conditionals in Eqs. (34) and (35).

$$P_{E_{f,a}} = 10 \frac{|E_{0,d} - E_{f,a}|}{E_{0,d}} \tag{36}$$

$$P_{\gamma_{f,a}} = 10 \frac{|\gamma_{0,d} - \gamma_{f,a}|}{\gamma_{0,d}} \tag{37}$$

Additional penalties are imposed on decoupled ascent trajectories. Shown in Eqs. (36) and (37), these are intended to connect the final specific energy and flight-path angle of the ascent phase to target values corresponding to initial values of the descent phase.

5 Design Space Exploration

The design space is understood to be prohibitively large, as it is not possible to evaluate all combinations within a parameter set. Furthermore, the problem is not well understood given that this particular implementation of the reference vehicle has not been previously evaluated. Thus, a variety of Monte-Carlo evaluations were initially performed to guide the selection of individuals for the initial populations and to inform the ranges of the decision vector parameters. This exercise was done in an effort to improve the effectiveness of the optimisation process of both the design space exploration and the trajectory optimisation itself.

Figure 8 shows the results of a Monte-Carlo evaluation. This test was completed for an unconstrained run of a coupled trajectory type, a population of 100,000 individuals with five (5) control nodes, which were randomly selected from a uniform distribution with a given random seed. The propagation/guidance step sizes of 1 s were selected to reduce the computational load while remaining within the vehicle's validated performance capabilities.

Figure 8a shows a distribution of values whose ranges for the maximum body frame mechanical load are significantly higher than desired (much greater than 1 g_0) while also remaining far from the intended target. In fact, the figure shows a high concentration of individuals with n_{max} of about 5 g_0 that reached a minimum angular distance from the central target of about 48°. This observation is confirmed by the top left chart of the violation histograms shown in Fig. 8b, further illustrating the low probability of randomly identifying feasible individuals.

A design space exploration is performed to evaluate the effectiveness of a variety of optimisation approaches. This will be done by evaluating various of the optimisers available in PaGMO with a series of combinations of initial population
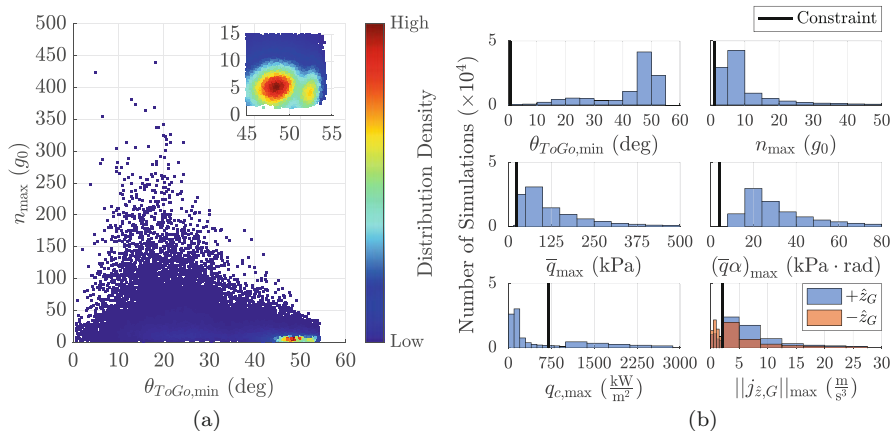
Fig. 8 Uniformly distributed random individuals with initial random seed 1 and 5 control nodes. (**a**) Variable comparison. (**b**) Violation histogram

Table 7 Fitness vector terms per objective function case (OFC)

Term	Eq.	Type	Objective function case													
			A	B	C	D	E	F	G	H	I	J	K	L	M[a]	N
Angular distance-to-go	(30)	C	x	x	x	x	x	x	x	x	x	x	x	x	x	x
Fuel mass	(31)	C									x					x
Heat load	(32)	C							x	x					x	x
Total g_0-Load	(33)	V		x	x	x	x	x	x	x	x					
Dynamic pressure	(33)	V			x	x	x	x	x	x	x					
Bending moment	(33)	V				x	x	x	x	x	x					
Heat flux	(33)	V					x	x	x	x	x					
Flight-path angle	(34)	P						x	x	x	x		x			
Monotonic energy state	(35)	P							x	x	x					
Grouping 1[b]	–	V										x	x	x	x	x
Grouping 2[c]	–	P											x	x	x
Decoupled ascent $E_{f,a}$	(36)	P[d]	x	x	x	x	x	x	x	x	x	x	x	x	x	x
Decoupled ascent $\gamma_{f,a}$	(37)	P[d]	x	x	x	x	x	x	x	x	x	x	x	x	x	x

Term Types: Cost (C), Constraint Violation (V), and Penalty (P)
[a] OFC-**M**.1 augments the total g_0-load violation by a factor of 10
[b] Grouping 1 is composed of all V-type terms
[c] Grouping 2 is composed of all P-type terms
[d] Applied when linking decoupled phases

sources, a number of control nodes, initial random seed initialisers, objective function cases, single- vs multi-objective, and constrained vs unconstrained. The objective function cases are defined in Table 7, where they are composed of different combinations of the costs, constraint violations, and penalties introduced in Sect. 4.

Table 8 Design space exploration factors to investigate

Factor	Options
Number of nodes	[5, 6, 7]
PRNG seed initialiser	[234998684, 88236, 5927502]
Initial populations	PRNG vs. Individual ranking
Number of objectives	Single vs. Multi/many
Constraint Type	Unconstrained vs. Constrained
Optimization algorithm	NSGA-II, MOEA/D (DE), IHS
Objective function case	OFC-**A** to OFC-**N** (Table 7)

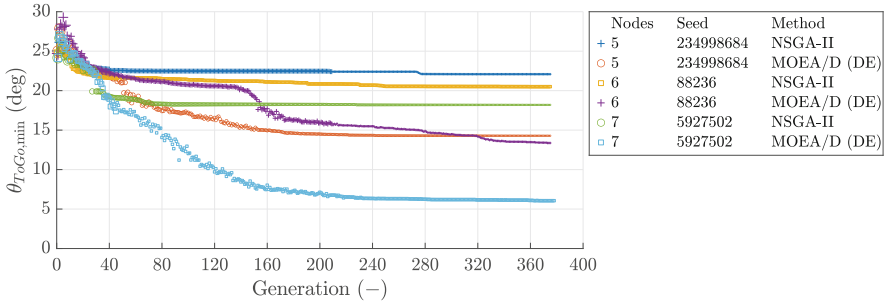| Nodes	Seed	Method
+ 5	234998684	NSGA-II
○ 5	234998684	MOEA/D (DE)
□ 6	88236	NSGA-II
+ 6	88236	MOEA/D (DE)
○ 7	5927502	NSGA-II
□ 7	5927502	MOEA/D (DE)

Fig. 9 Generational history of $\theta_{ToGo,\min}$ for an unconstrained single-objective coupled (ascent phase only), OFC-**A**, and initial population sourced from fitness vector ranking

With the factors presented in Table 8, the design space exploration optimisations had a maximum number of generations of $N_{max} = 500$ with a minimum equal to 75% of the maximum. Within the 75% and 100%, the optimisation continued until the change of the population's average fitness was negligible.

Figure 9 and Table 9 present an excerpt of the variety of summarising tools created to analyse the data. Figure 9 shows the generational history of $\theta_{ToGo,\min}$ corresponding to the population's top individual for a variety of factors and an OFC-**A**. It is possible to observe how, with this particular set of cases, NSGA-II [1] had an overall tendency to converge to a much higher $\theta_{ToGo,\min}$, whereas MOEA/D (DE) [2] was able to reach lower values. Within MOEA/D (DE), it is also possible to see reduced $\theta_{ToGo,\min}$ as the number of control nodes increased. Additionally, the MOEA/D (DE) profiles show signs of increased diversity as the overall $\theta_{ToGo,\min}$ is reduced. This can be observed by the 'noise' as the overall trends continue to decrease the $\theta_{ToGo,\min}$. Table 9 presents a summary of the minimum values of the constrained variables for various objective function cases with the MOEA/D (DE) genetic algorithm. The colour coding corresponds to the number of nodes that produced the minimum value.

It is clear that the numerous evaluations resulting from the combination of factors being investigated (see Table 8) yield a dataset from which drawing conclusions becomes a challenge. As a result, key indicators were used to draw conclusions due to the overall complexity of the data. Among them was the consistency of satisfying

Table 9 Coupled ascent phase constrained multi-objective: MOEA/D (DE). Population sourced from fitness vector ranking

MOEA/D (DE)

Objective Function Case		B	C	D	E	F	G	H	I	J	K	L	M	N
$\sigma_{\lvert fitness\rvert}$	**5**	19.02	9.11	18.32	20.09	498.6	16.66	13.82	926.0	277.2	441.0	8.68	330.8	567.8
	6	18.90	13.15	14.71	16.76	18.52	16.52	760.1	344.5	13.19	16.40	19.42	907.8	406.8
	7	10.70	23.27	22.10	12.63	17.33	398.3	1269	1210	13.23	19.48	16.18	14.54	17.24

Variable	Units	S.F.	B	C	D	E	F	G	H	I	J	K	L	M	N
			Scaled variable minimum per objective function case												
θ_{ToGo}	deg	3.37	1.01	1.00	1.02	1.10	3.59	1.17	8.31	3.40	4.00	1.06	2.20	1.27	1.46
n	g_0	1.55	1.67	1.53	1.17	1.11	1.24	1.56	1.44	1.12	1.00	1.37	1.61	1.17	1.18
$\bar{q}$	kPa	14.3	1.00	1.09	1.03	1.00	1.00	1.19	1.00	1.00	1.00	1.00	1.00	1.00	1.00
$\bar{q}\alpha$	kPa·rad	2.83	1.65	1.69	1.56	1.60	1.47	1.76	1.64	1.35	1.41	1.37	1.42	1.00	1.26
q_c	kW/m²	118.4	11.13	12.72	12.27	5.29	6.85	6.85	2.56	5.67	5.70	2.31	2.51	6.44	1.00
Q	MJ/m²	21.73	17.96	23.26	32.40	7.83	10.03	3.95	4.38	6.02	9.98	2.22	2.39	9.12	1.00

$\sigma_{\lvert fitness\rvert}$ = Fitness magnitude standard deviation

S.F. = Scaling Factor = Variable minimum among all objective function cases

Variable minimum as achieved by
= 5 nodes
= 6 nodes
= 7 nodes

Table 10 Trajectory optimisation input parameters

Parameter	Selection
Population size	100
Population source	Fitness vector ranking
Max. generations	$3000 \rightarrow 100$
Control nodes	7
Objective type	Multiple
Objective function case	OFC-N^a
Optimising Algorithm	MOEA/D (DE)
Time steps ($\Delta t_p | \Delta t_g$)	$1s \rightarrow 0.05s$	$1s \rightarrow 0.1s$

Arrow ($\rightarrow$): general then localised optimisation
[a] Parallel evaluation will be done with OFC-**I**

constraints with the recurrence of low maximum values, reduced dimensionality in both decision vector and fitness vector space, and the population's diversity.

Table 10 presents a summary of the resulting optimization primary parameters to be used for the optimisation of both coupled and decoupled trajectories. From these parameters, the maximum number of generations and the propagation and guidance time steps (Δt_p and Δt_g) show two sets, corresponding to the initial optimisation and a localised refined optimisation.

6 Trajectory Optimisation

The trajectory optimisation was performed with two separate approaches. The decoupled approach, presented in Sect. 6.1, begins with the parallel evaluation of a descent phase optimisation with five different starting points defined by $\hat{\theta}_{ToGo,i}$. The initial conditions of these evaluations are then analysed with the purpose of extracting terminal state target values for ascent phase optimisations. These evaluations are then intended to be linked such that a continuous trajectory would then be generated. Details and analysis are presented throughout the section leading to the conclusion that a continuous trajectory was not found.

Section 6.2, on the other hand, presents the coupled approach, where a general optimisation is performed and then followed by a localised optimisation. The section then discusses the resulting sub-optimal individual found from the approach.

6.1 Decoupled Approach

Following the parameter bounds introduced in Table 3 and the optimisation parameters detailed in Table 10, the decoupled approach begins by evaluating the descent phase at five different decoupled descent distance-to-go ratios. These evaluations
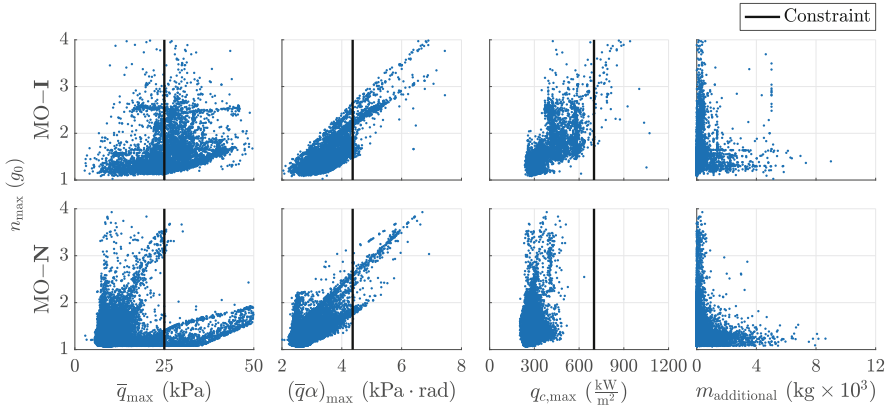
Fig. 10 Decoupled descent single- and multi-objective (SO & MO) variable comparisons at TAEM for OFC-**I** and OFC-**N** with $\hat{\theta}_{ToGo,i} = 0.30$
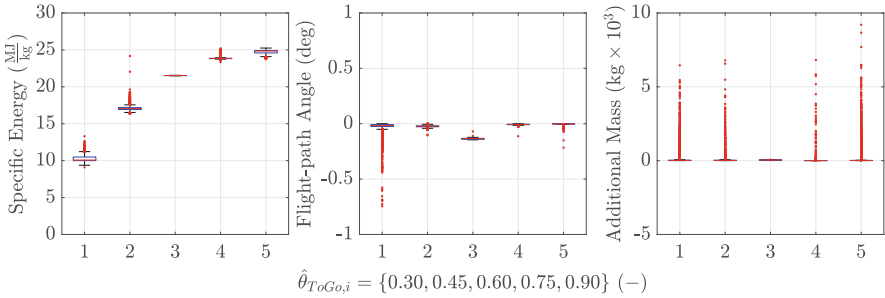

Fig. 11 Boxplots of phase change values of filtered individuals for all $\hat{\theta}_{ToGo,i}$

were initialised with $\hat{\theta}_{ToGo,i} = \{0.30, 0.45, 0.60, 0.75, 0.90\}$ and yielded numerous individuals that satisfied most of the operational constraints shown in Table 6.

Figure 10 shows the maximum g_0-load throughout the decoupled decent phase compared to the maximum values for dynamic pressure, bending moment, and stagnation heat flux. These point clouds show the resulting individuals throughout all generations that have reached the TAEM. As calculated, a significant portion of the population was close to the 1-g_0 constraint. Similar distributions were observed for all other $\hat{\theta}_{ToGo,i}$, though with reduced total populations as $\hat{\theta}_{ToGo,i}$ increased. This was to be expected as larger $\hat{\theta}_{ToGo,i}$ mean larger initial angular distances-to-go at the start of the decoupled descent phase.

The selection criteria from all individuals that reached the TAEM include the satisfaction of all constraints presented in Table 6 with the distinction of $n_{\max} \leq 1.15\ g_0$. The initial specific energy $E_{0,d}$, initial flight-path angles $\gamma_{0,d}$, and additional mass of the individuals selected from the decoupled descent phase are presented in Fig. 11.

The figure shows the distribution of the values as boxplots for each $\hat{\theta}_{ToGo,i}$. These boxplots illustrate the distribution of data through its quartiles, where outliers are depicted at red discreet points beyond the black lines. The 25th and 75th percentiles are, respectively, illustrated by the lower and upper bounds of each blue box, and the sample's median (50th percentile) is shown as the single red line within each box.

The distributions show an increase of the initial specific energy as $\hat{\theta}_{ToGo,i}$ increases, which is to be expected. Curiously, the case of $\hat{\theta}_{ToGo,i} = 0.60$ yielded values that were within the trend yet with an increasingly small spread, indicating a significantly small population compared to the other cases. A possible explanation would be need for additional generations to increase the total individuals found.

The initial decoupled descent flight-path angles were observed to have a trend towards zero. Though the parameter's upper bound was fixed at $\gamma_{0,d,max} = 0$, there were clear outliers, especially for the case of $\hat{\theta}_{ToGo,i} = 0.30$. These outliers can be explained by the understanding that the closer the vehicle is to the TAEM, the lower the need for an extended downrange, hence the possibility of a more negative initial flight-path angle. Additional to the outliers, the case of $\hat{\theta}_{ToGo,i} = 0.60$ shows a median lower than -0.1 deg. However, all values are within a relatively close distance from zero, which would be compatible with the goal of minimising mechanical loads throughout the trajectory.

All decoupled decent cases had a tendency to minimise the additional mass to the point of being borderline negligible. Since the effect of the additional mass parameter on the decoupled descent cases was to increase the total dry mass of the vehicle, there was a possibility that the parameter was unnecessarily limiting the optimisation. Understanding that there was a minimum dry mass (nominal dry mass of the vehicle), this driver to have almost negligible additional mass opened up the possibility of the optimiser driving the system to a configuration that carried the nominal fuel mass or less. However, the spread of outliers indicates a possibility of potential individuals with additional mass. This led to the definition of three mass cases for the decoupled ascent optimisation: minimised additional mass, nominal fuel mass, and minimised fuel mass.

The median values of the selected initial decoupled descent specific energy and flight-path angle ($E_{0,d}$ and $\gamma_{0,d}$) were then taken as optimisation targets for the final state of the decoupled ascent phase as $E_{f,a}$ and $\gamma_{f,a}$, along with the values of the corresponding trajectory linking parameters introduced in Table 3. The optimisation parameters for the decoupled ascent phase were the same as for the decoupled descent, shown in Table 10. Once evaluated, the selection criteria for all mass cases required a relaxed maximum n_{max} of 1.50 g_0. This was due to the lack of individuals that had reached their corresponding transition point ($\hat{\theta}_{ToGo} = \hat{\theta}_{ToGo,i}$) with tighter constraints.

The distributions of specific energy at the end the decoupled ascent phase ($\hat{\theta}_{ToGo} = \hat{\theta}_{ToGo,i}$) are shown in the left plot of Fig. 12, with ascent optimisation targets as black lines. The most significant observation is that none of the distributions reached the targeted specific energy levels. Most of the distributions followed
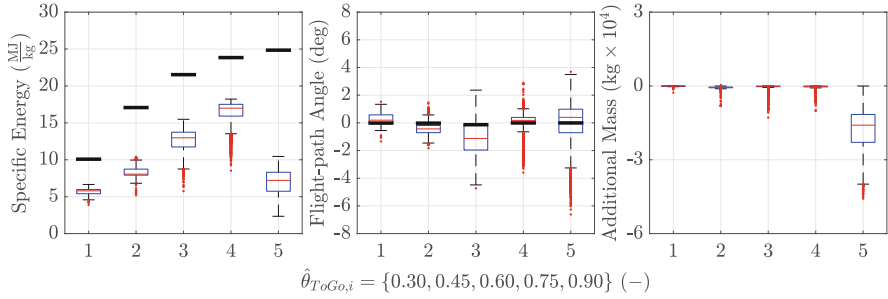
Fig. 12 Decoupled ascent transition point boxplots of filtered individuals for various $\hat{\theta}_{ToGo,i}$ for minimised fuel mass and $n_{\max} \leq 1.50\, g_0$. Ascent optimisation targets shown in black lines

the decreasing trend of the target energy levels as $\hat{\theta}_{ToGo,i}$ decreased. However, the case of $\hat{\theta}_{ToGo,i} = 0.90$ was not only significantly lower than the required target but it did not follow the decreasing trend. It is understood that this phenomenon occurs due to the selection of the individuals with a reduced $n_{\max}$ that have reached $\hat{\theta}_{ToGo} = 0.90$, while they have not had the temporal nor spatial opportunity, or need, to convert the propellant mass' energy into kinetic and potential energy. Simply put, the vehicle reaches the phase transition point too fast without the need to consume more propellant. Though it is clear that there could be a larger conversion of energy within the relatively short distance, especially with the available propellant, it is expected that the g_0-loads would be significantly larger. This ultimately would exclude these individuals from the distributions of interest. Regarding the transition point flight-path angles, the largest variation was brought about by $\hat{\theta}_{ToGo,i} = 0.90$, also pointing to the difficulty of identifying individuals that can reach the required specific energy levels without extreme $n_{\max}$ values. Though not illustrated, all mass cases showed an overall tendency towards the nominal mass configuration, which shows a preference of a lighter vehicle to reduce the maximum g_0-loads during the ascent phase.

From these distributions, it can be said that the decoupled ascent optimisation process successfully drives the populations to the desired phase transition point ($\hat{\theta}_{ToGo} = \hat{\theta}_{ToGo,i}$) yet is unable to produce the specific energy targets required by the decoupled descent optimisation with reduced $n_{\max}$. Though the actual fuel consumption and time histories are not discussed, the fact remains that the current decoupling of the search space drives the descent phase optimisation into a region of the design space that does not intersect with the region where the decoupled ascent phase optimisation yields lower $n_{\max}$ values. This is a reasonable conclusion, given that the decoupled descent optimisation does not have a strong link to the decoupled ascent phase optimisation. Hence, a functional relationship is not available with which the optimisation process can guide the populations towards regions that are intersecting. As such, a linkable decoupled trajectory was not identified.

6.2 Coupled Approach

The coupled approached optimisation was performed according to the optimisation parameters shown in Table 10. Figure 13 shows the maximum g_0-load throughout the entire trajectory compared to the maximum values for dynamic pressure, bending moment, and stagnation heat flux. These point clouds show the resulting individuals throughout all generations that have reached the TAEM. The lower row shows that with OFC-**N** the maximum dynamic pressures satisfied the constraint with sufficient margin, unlike the corresponding decoupled descent phase. The maximum bending moments had a spread across the constraint line that was skewed towards satisfying the constraint, and unlike the decoupled decent phase, the heat flux had a larger concentration around the constraint line. Unlike with the decoupled approach, the separate phases of the coupled approach did not produce trajectories with max g_0-loads approaching values as close to 1 g_0.

A sub-optimal individual was identified from the point clouds, as shown in Fig. 14 with the red dot. This value, denoted as $n_{max,min}$ for the minimum of the maximum g_0-loads, was found to be 1.19 g_0. When comparing the relative location of the red dot within the distributions of each of the variables shown in Fig. 14, the maximum bending moment is approximate to its median, whereas the maximum heat flux is closer to the left tail of the distribution. The additional mass, however, is at approximately 5500 kg and towards the right tail of the distribution.

To further drive the loads towards the constraint of 1 g_0, the sub-optimal point was then used as a reference for local optimisation. The decision vector was expanded by 1-, 2-, 5-, and 10%, and a Monte-Carlo test was performed with 5000 individuals and refined time steps of $\Delta t_p = 0.05$ s and $\Delta t_g = 0.1$ s. Not only did this not drive the $n_{max,min}$ of the population closer to the constraint, but many individuals did not reach the TAEM. This may imply that the optimisation process had already
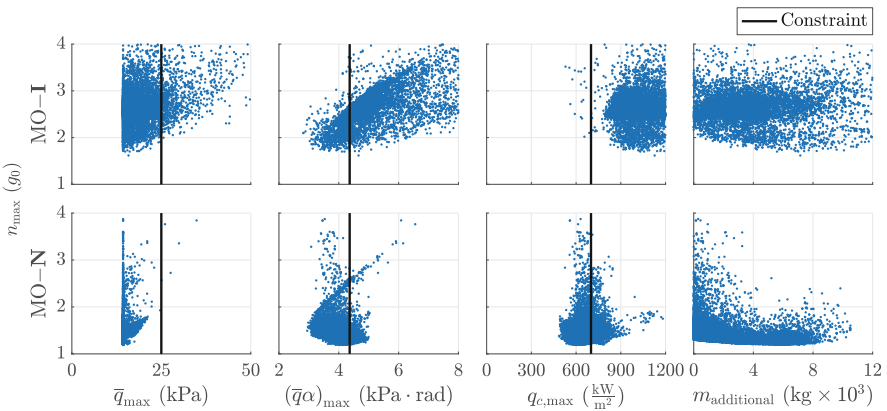

Fig. 13 Coupled trajectory single- and multi-objective (SO & MO) variable comparisons at TAEM for OFC-**I** and OFC-**N**
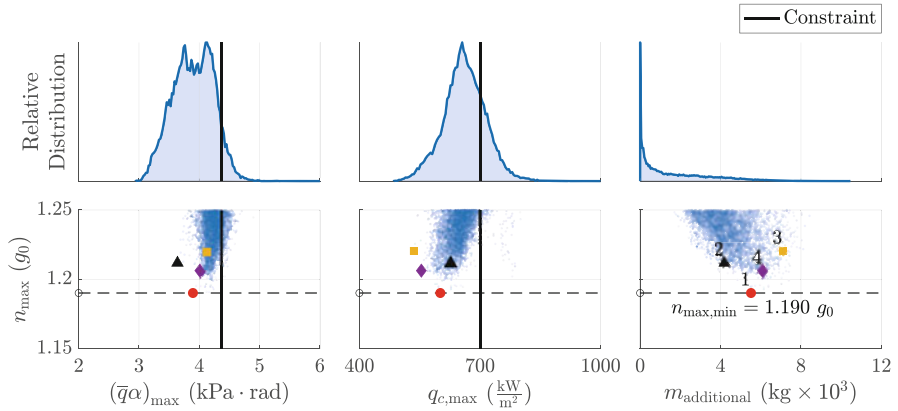
Fig. 14 Identification of sub-optimal and reference individuals used for localised global optimisation

converged to a small region and/or the result of the tests were a replication of the observations from the initial Monte-Carlo design space exploration with 100,000 individuals. This led to the localised optimisation of the population to be with the same global optimisation method (MOEA/D (DE)), albeit with a reduced design space.

The objective function cases evaluated were OFC-**N** and OFC-**M**.1. The selection of OFC-**N** was to maintain continuity with the initial evaluation. The $n_{max} - m_{additional}$ Pareto front showed a well-behaved trend where an increase in $m_{additional}$ indicated a possible reduction in n_{max}. This led to the creation and selection of OFC-**M**.1, where the mass cost is no longer included and the total g_0-load constraint violation was increased by an order of magnitude.

The reference points were selected along the $n_{max} - (\bar{q}\alpha)_{max}$ and $n_{max} - q_{c,max}$ Pareto fronts. Including $n_{max,min}$, a total of four points were selected, as shown in Fig. 14 by the numeric labels in the bottom right panel. Each case had a set of parameter bounds created by expanding the decision vector of each individual identified in Fig. 14. A decision vector expansion of 5% was chosen because it brought about the most individuals to the TAEM with the localised Monte-Carlo tests. However, the $m_{additional}$ was arbitrarily defined to have a range of [4000, 15,000] kg. The initial populations used to seed the localised global optimisation were determined by identifying the individuals that produced the lowest 100 n_{max} from the general global optimisation. The maximum number of generations was set to 100.

Figure 15 illustrates the variable comparisons of all individuals that reached the TAEM for two cases. The relevant reference individual is identified in the top left corner of the first panel of each row, and its corresponding placement in each panel is identified by the intersection of the dashed lines. OFC-**N** is presented in green asterisks and OFC-**M**.1 is presented as dark red squares. It is possible to see in the figure how each objective function case drives the populations in different
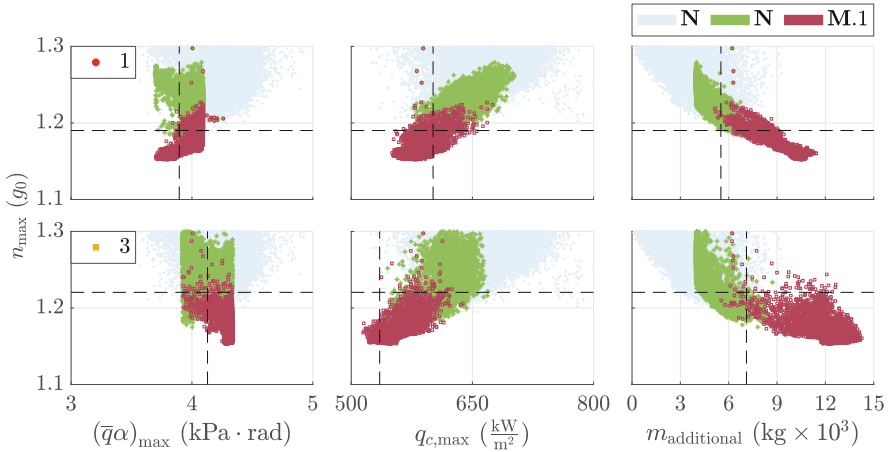
Fig. 15 Localised multi-objective optimisation variable comparisons for OFC-**N** and OFC-**M**.1

directions. OFC-**N** did not significantly drive n_{max} values closer to 1 g_0. It can also be seen that this case had a clear tendency of minimising $m_{additional}$, as it drove the populations towards the lower bound of 4000 kg. OFC-**M**.1, on the other hand, was able drive n_{max} values further towards the 1 g_0 constraint. However, this was achieved at the expense of significantly increasing $m_{additional}$.

The $n_{max} - m_{additional}$ front was chosen for further analysis. The selection was based on the relatively well-behaved curve and the fact that $m_{additional}$ is a known input parameter. The improvement on n_{max} can be clearly visualised in Fig. 16, where all localised global optimisation populations are aggregated over the general TAEM population. The figure shows the distributions of each objective function case for $m_{additional}$ in the top panel and for n_{max} on the right panel. The additional mass distributions for OFC-**N** (blue and green areas) show a trend towards their minimum bounds (0 kg and 4000 kg). The distribution of OFC-**M**.1 (red area) has a large spread with a larger proportion around 10,500 kg. The corresponding distributions for n_{max} show that only OFC-**M**.1 was able drive the population towards a lower n_{max}. The lowest value is identified as n_{max,min_2} with the second red dot and a value of 1.152 g_0. It is also possible to see that $m_{additional}$ values larger than 10,500 kg only increased n_{max}, suggesting that further improvement in this relation was no longer possible. In short, though there is a clear improvement in n_{max}, the difference is effectively negligible and comes at the need of a significantly higher additional mass.

Three Pareto fronts are also shown in Fig. 16. Though the left portions of the Pareto fronts were from the initial optimisation, it can be seen that as the additional mass increased, the Pareto points were increasingly selected from the local optimisations. Visual comparisons of their decision vectors, trajectory data, and variable time histories showed relatively small differences for the individuals near n_{max,min_2}. In fact, other than for $m_{additional}$, the decision vectors showed characteristics of
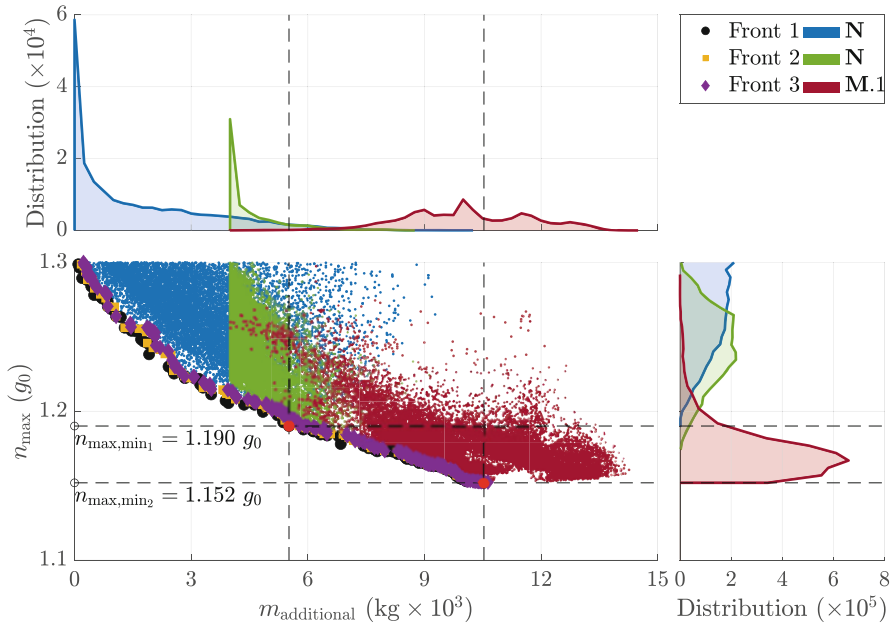
Fig. 16 Pareto front of maximum g_0-load vs. additional mass, including general (OFC-**N**) and local optimisations (OFC-**N** and OFC-**M**.1)
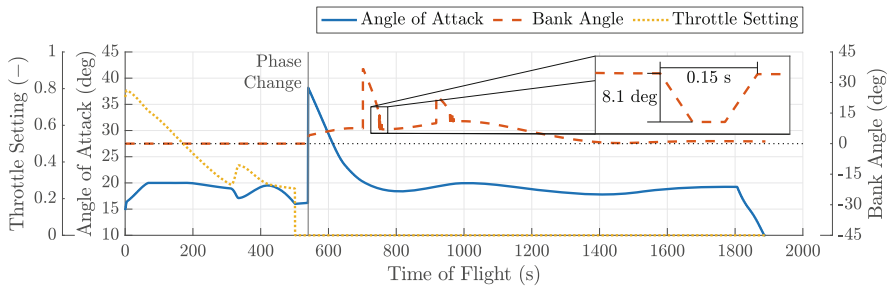

Fig. 17 'Best' individual time history: control variables

clustering. However, as a sensitivity analysis has not been completed by modelling realistic uncertainties, it is unclear how deviations from the clusters may affect the resulting trajectories.

Figure 17 shows the time histories of the control variables. Angle of attack, shown in solid blue, presents a saturated segment during the ascent phase, a significant spike during the phase change that is eased off during the initial descent and a steep decrease at the end. The steep decrease at the end is a result of the vehicle's aerodynamic envelope at lower Mach numbers (see Fig. 1c). The bank angle, shown in the dashed red line, is zero during the ascent phase and positive
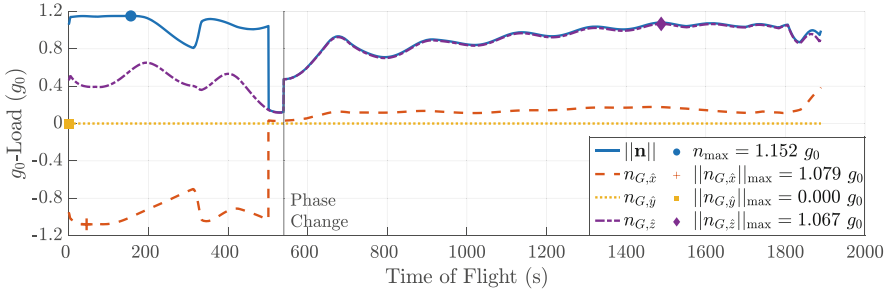
Fig. 18 'Best' individual time history: g_0-loads

during the descent phase. This particular profile implies that the vehicle did not perform a bank reversal. Additionally, there are two spikes with certain oscillations occurring as they revert to the lower trend. The large spikes are the result of the skip suppression, where the bank angle required to avoid skipping is commanded if $\gamma \geq 0$ and $\dot{\gamma} \geq 0$. The oscillations are the natural consequence of the vehicle's flight-path angle and its time rate of change as the trajectory maintains a horizontal or slightly negative path. However, the largest oscillation, shown on the inset, is relatively short-lived. Though the values have an effect on the calculated trajectory, these oscillations would not be feasibly executed if a controlled flight is performed. The throttle setting, shown as the yellow dotted line, has an initial decreasing trend that is shortly interrupted and then continues to decrease. The throttle setting then has a sudden reduction to zero, engine shut-off, prior to terminating the ascent phase. This confirms the hypothesis about thrust being present exclusively during the ascent phase. As the ascent phase extracts the fuel mass's energy, it is also expected that higher mechanical loads would be experienced by passengers during the initial phase of the coupled trajectory.

The overall decreasing trend of the throttle setting works in concert with the angle of attack in maintaining a relatively low g_0-load. Figure 18 illustrates the g_0-load magnitude and its components in the passenger frame, $\mathcal{F}_G$. The figure also shows the points of maximum absolute values. The g_0-load magnitude, shown in solid blue, presents the maximum value of 1.152 g_0. Prior to that point, there is a relatively constant line. However, these values are due to an exchange in component distribution along the $\mathcal{F}_{G,\hat{x}}$ and $\mathcal{F}_{G,\hat{z}}$ axes. The value has a short decrease and goes below 1 g_0 during a pull-up manoeuver where the angle of attack and throttle setting both decrease. However, when they increase again, the total g_0-load increases to over 1 g_0. The value then shows a short undulation before having a sharp decrease prior to the phase change. Once in the descent phase, the total g_0-load has a step increase to about 0.5 g_0 prior to showing an undulating trend that eventually goes above 1 g_0 for almost the remainder of the trajectory. This undulation along $\mathcal{F}_{G,\hat{z}}$ can be traced to the vehicle's height, flight-path angle, and flight-path angle rate (all during descent). Throughout the trajectory, the $\mathcal{F}_{G,\hat{x}}$ axis dominates during the ascent phase, while the $\mathcal{F}_{G,\hat{z}}$ axis dominates during the descent phase. In fact, the
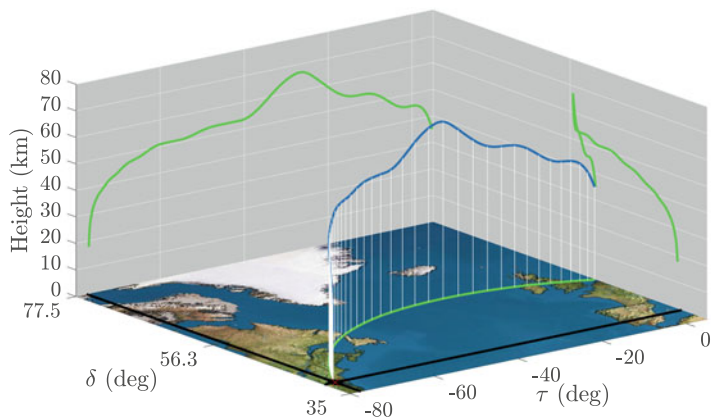
Fig. 19 'Best' individual height over planar trajectory

maximum absolute value of the ascent phase corresponds to $n_{G,\hat{x}} = -1.079\, g_0$ (red cross on red dashed line), while for the descent phase it corresponds to $n_{G,\hat{z}} = 1.067\, g_0$ (purple diamond on purple semi-dashed line). These directional maxima are not entirely sustained as they occur within flight segments that are within clear violation of the 1 g_0 constraint. The extended exposure during ascent lasts about 160 s and about 400 s during descent.

The vehicle's trajectory is shown in Fig. 19, with its height over a planar trajectory. Of note is the geographic path of the ground track, where the ascent phase occurs above the region associated with the United Kingdom and the descent phase occurs largely above the northeastern coast of the USA. Furthermore, the lack of bank reversals can be seen as the vehicle aims to the circle defined by the TAEM. Though not shown, numerous other trajectories presented similar characteristics.

7 Concluding Remarks

The overall exercise could be described in four main segments: development of a trajectory simulator with the identification of key generalised parameters; objective function case definition with a variety of costs, constraint violations, and penalties; design space exploration with different factors, dimensionality considerations, and objective function cases; and trajectory optimisation execution with subsequent localised exploitation.

The key generalised parameters used in the trajectory simulator allowed for the evaluation of ascent and descent profiles with different expected dynamics, albeit at the expense of increased dimensionality. Similarly, though defining the objective functions and their combinations required a certain degree of creativity, it was ultimately their influence on the optimisation that was of both concern and interest.

The design space exploration executed was an important step in the process. Though the number of factors investigated brought forth a complex dataset, it did allow for an improved understanding of the capabilities and limitations of the factors as applied to the current problem. Visualising and summarising the exploration data with the ultimate goal of identifying preferred factors for trajectory optimisation is a challenging task that must be done with care and caution. However, the conclusions drawn from the observations are understood to shed light on the problem and provide a reference for future studies. These include the implementation of node control, objective function case, and the optimisation algorithm selected.

The execution of the trajectory optimisation follows relatively easily once an increased confidence in the understanding of the design space is acquired. In fact, this understanding can be used to further exploit the design space, as performed with the localised global optimisation with the *coupled* phase approach. It was possible to see the $n_{\max} - m_{\mathrm{additional}}$ front required a significant increase in additional mass to reduce the $n_{\max}$. This is understood to be a natural consequence of the decreasing throttling required to sufficiently accelerate the vehicle to reach the TAEM while minimising the $n_{\max}$ experienced throughout the trajectory (i.e. longer thrust time with variable mass flow rate).

That being so, the *decoupled* phase approach was unable to generate linkable trajectories, which is understood to have been due to the optimiser driving the populations of the separate optimisations to regions that did not intersect. Though the reason may be due to a lack of sufficient implicit linking qualities or the decoupling rationale, it may also be due to the ranges of parameter bounds and the selection of the objective function case.

Overall, the problem structure is understood to drive a given population towards characteristics of interest if sufficient phase coupling is considered. That is to say that though phase decoupling may be initially preferred due to a reduced design space, the complex non-linear dynamics of the problem may still require the evaluation of coupled phases if conditions cannot be ensured for decoupling.

Ultimately, though the *coupled* approach did require a significant increase in additional mass for the chosen route and vehicle, the result does indicate the possibility of using the approach to identify a set of parameters that could drive the optimal design of a vehicular configuration and associated route such that an individual could participate in hypersonic travel without health screenings.

Among the recommendations to further study are the augmentation of the equations of motion and GNC module to consider a more realistic flight; the evaluation of alternate optimisers; other vehicular configurations and propulsive systems and the inclusion of no-fly zones.

References

1. Deb, K. and Pratap, A. and Agarwal, S. and Meyarivan, T., "A Fast and Elitist Multiobjective Genetic Algorithm: NSGA-II", *IEEE Transactions on Evolutionary Computation*, Vol. 6, No. 2, pp. 182–197, 2002.

2. Zhang, Q. and Li, H., "MOEA/D: A Multiobjective Evolutionary Algorithm Based on Decomposition", *IEEE Transactions on Evolutionary Computation*, Vol. 11, No. 2, pp. 712–731, 2007.
3. Biscani, F. and Izzo, D. and Yam, C. H., "A Global Optimisation Toolbox for Massively Parallel Engineering Optimisation", *ArXiv e-prints*, 2010.
4. Mooij, E. and Hänninen, P.G., "Distributed Global Trajectory Optimization of a Moderate Lift-to-Drag Re-Entry Vehicle", *AIAA Guidance, Navigation, and Control Conference*, 2009.
5. Dijkstra, M. and Mooij, E. and Sudmeijer, K., "Trajectory Optimization to Support the Study of Hypersonic Aerothermodynamic Phenomena", *AIAA Atmospheric Flight Mechanics (AFM) Conference, Guidance, Navigation, and Control and Co-located Conferences*, 2013.
6. Hess, Jaimy and Mooij, Erwin, "Node Control and Numerical Optimization of Aerogravity-Assist Trajectories", *AIAA Atmospheric Flight Mechanics Conference*, 2017.
7. Koelle, D. E. and Kuczera, H., "Sänger II, an advanced launcher system for Europe", *Acta Astronautica*, Vol. 19, No. 1, pp. 63–72, 1989.
8. MBB, "Study on Re-entry Guidance and Control - Final Report, Vol. 2, Reference Vehicle Definition and Orbital Constraints", *MBB Space Communication and Propulsion Systems Division*, TN-ESA 6718/85-1, Rev. A. 1988.
9. Mooij, E., "The HORUS-2B Reference Vehicle", *Delft University of Technology*, Memorandum M-682, 1995.
10. Koelle, D. E. and Kuczera, H., "Sänger Space Transportation System - Progress Report", *41st International Astronautical Congress, International Astronautical Congress (IAF)*, IAF-90-175. 1990.
11. Yoder, C. F., "Astrometric and Geodetic Properties of Earth and the Solar System", *Global Earth Physics: A Handbook of Physical Constants*, AGU Reference Shelf 1, American Geophysical Union, 1995.
12. Regan, F. J. and Anandakrishnan, S. M., "Dynamics of Atmospheric Re-Entry", 1st ed, *AIAA*, AIAA Education Series, 1993.
13. Chapman, D. R., "An Approximate Analytical Method for Studying Entry into Planetary Atmospheres", *NACA - Scientific and Technical Information Division*, NACA-TN-4276, 1958.
14. Tauber, M. E. and Menees, G. P. and Edelman, H.G., "Aerothermodynamics of Transatmospheric Vehicles", *Journal of Aircraft*, Vol. 24, No. 9, pp. 594–602, 1987.
15. Moore, T. E., "Space Shuttle Entry Terminal Area Energy Management", *Washington, DC: National Aeronautics and Space Administration, Lyndon B. Johnson Space Center*, NASA Technical Memorandum 104744 1991.
16. Han, X. and Guo, X., "Cubic Hermite interpolation with minimal derivative oscillation", *Journal of Computational and Applied Mathematics*, Vol. 331, pp. 82–87, 2018.
17. Vinh, N. X. and Busemann, A. and Culp, R. D., "Hypersonic Planetary Entry Flight Mechanics", *The University of Michigan Press*, 1980.
18. Dirkx, D. and Mooij, E., "Optimization of entry-vehicle shapes during conceptual design", *Acta Astronautica*, Vol. 94, No. 1, pp. 198–214, 2014.
19. ISO, "Measurement of ride quality - Part 1: Lifts (elevators), *International Organization for Standardization*, ISO 18738-1:2012(en), 2012.